

H2AX chromatin structures and their response to DNA damage revealed by 4Pi microscopy

Jörg Bewersdorf*, Brian T. Bennett^{†‡}, and Kendall L. Knight^{†§}

*Institute for Molecular Biophysics, The Jackson Laboratory, 600 Main Street, Bar Harbor, ME 04609; [†]Department of Biochemistry and Molecular Pharmacology, Aaron Lazare Medical Research Building, 364 Plantation Street, University of Massachusetts Medical School, Worcester, MA 01655; and [‡]Leica Microsystems Inc., 410 Eagleview Boulevard, Exton, PA 19341

Communicated by Robert T. Sauer, Massachusetts Institute of Technology, Cambridge, MA, October 2, 2006 (received for review August 16, 2006)

DNA double-strand breaks (DSBs) caused by cellular exposure to genotoxic agents or produced by inherent metabolic processes initiate a rapid and highly coordinated series of molecular events resulting in DNA damage signaling and repair. Phosphorylation of histone H2AX to form γ -H2AX is one of the earliest of these events and is important for coordination of signaling and repair activities. An intriguing aspect of H2AX phosphorylation is that γ -H2AX spreads a limited distance up to 1–2 Mbp from the site of a DNA break in mammalian cells. However, neither the distribution of H2AX throughout the genome nor the mechanism that defines the boundary of γ -H2AX spreading have yet been described. Here, we report the identification of previously undescribed H2AX chromatin structures by successfully applying 4Pi microscopy to visualize endogenous nuclear proteins. Our observations suggest that H2AX is not distributed randomly throughout bulk chromatin, rather it exists in distinct clusters that themselves are uniformly distributed within the nuclear volume. These data support a model in which the size and distribution of H2AX clusters define the boundaries of γ -H2AX spreading and also may provide a platform for the immediate and robust response observed after DNA damage.

γ -H2AX | H2AX chromatin clusters | super-resolution 4Pi microscopy | chromatin response to DNA damage | 3D quantification of chromatin structures

Maintenance of genome integrity is critical for organism development and survival, and higher organisms have evolved sophisticated mechanisms for detection and repair of chromosome breaks. DNA damage results in the rapid and coordinated action of various pathways, including activation of cell cycle checkpoints (1, 2), histone modification near the site of the break (3, 4), and recruitment of chromatin remodeling enzymes (4–6), cohesins (7–9), and DNA repair proteins (1, 2, 10). The significance of these molecular processes is highlighted by the fact that defects in many are associated with an increased risk of cancer and developmental and immunologic abnormalities (1). Important insights into the positioning of nuclear signaling and repair proteins and their response to various types and levels of genomic insults have been achieved by using immunofluorescence methods (10–12). However, it has been impossible to distinguish fluorescent signals in a three-dimensional (3D) environment that are closer together than 500–800 nm in distance given the depth resolution limits of current light microscopes. With \approx 100-nm resolution along the optic axis (*z* axis), 4Pi microscopy (13, 14) provides a significant increase in resolution and has allowed more defined images of cellular structures such as microtubules, mitochondria, or the Golgi apparatus (15). However, until now, imaging of endogenous nuclear proteins had not been achieved (a comparison of 4Pi vs. confocal is described in *Materials and Methods*). In this study, we describe the successful use of 4Pi microscopy to visualize endogenous nuclear proteins. By applying previously undescribed quantitative methods to the analysis of both confocal and 4Pi data, we have determined the local, global, and

relative 3D distribution of H2AX and γ -H2AX fluorescent signals in response to DNA damage and repair.

Results

Imaging of H2AX and γ -H2AX by Using 4Pi Microscopy. HeLa cells were fixed and stained for γ -H2AX and H2AX at 15, 45, 90, 180, 360, and 720 min after exposure to 3 Gy ionizing radiation (IR). Fig. 1 shows the 3D distribution of H2AX (green) and γ -H2AX (red) throughout HeLa nuclei at 15, 45, and 180 min after IR treatment (movies containing full 4Pi data sets for all six time points are Movies 1–6, which are published as supporting information on the PNAS web site). Several important observations come from visual inspection of the data. First, we find that H2AX appears in distinct clusters. Second, whereas the size of H2AX clusters remains relatively constant before and after IR exposure, γ -H2AX clusters grow in size up to \approx 90 min after IR. Third, H2AX and γ -H2AX clusters are dispersed throughout the entire nuclear volume. Finally, within the enhanced resolution limit of 4Pi microscopy, interestingly, we find very little to no coincident staining of H2AX and γ -H2AX at all time points before and after IR exposure. Quantitative analyses of these observations are described below.

Determination of H2AX and γ -H2AX Cluster Sizes. To clarify our observation regarding the cluster sizes for H2AX vs. γ -H2AX, 4Pi data were quantified by using an autocorrelation algorithm (see *Supporting Materials and Methods*, which is published as supporting information on the PNAS web site). The average diameter of H2AX clusters remained close to the technical resolution limit (<120 nm) throughout the entire time course (Fig. 2; see Fig. 6, which is published as supporting information on the PNAS web site). In contrast, the characteristic size of γ -H2AX clusters increased rapidly during the initial 90 min after IR, reaching a plateau of \approx 600-nm diameter from 6 to 12 h after IR. In mammalian cells, phosphorylation of H2AX is observed within the first minute after exposure to DNA-damaging agents and a $t_{1/2}$ has been estimated to be \approx 1 min, with maximum levels reached at 10–20 min (3, 16). Increases in γ -H2AX cluster size beyond this time (Figs. 2 and 6) can most reasonably be interpreted as resulting from localized chromatin expansion near the sites of breaks (17). The fact that we observe little to no change in the size of H2AX clusters or in their distribution throughout the 12-h time course (Figs. 1 and 2 and see below) argues against the idea that DNA damage induces large-scale chromatin movement (17) or accumulation of multiple breaks at a common site (18).

Author contributions: J.B. and B.T.B. contributed equally to this work; J.B. and B.T.B. designed research; J.B. and B.T.B. performed research; J.B., B.T.B., and K.L.K. analyzed data; and J.B., B.T.B., and K.L.K. wrote the paper.

The authors declare no conflict of interest.

Freely available online through the PNAS open access option.

Abbreviations: IR, ionizing radiation; PSF, point-spread function.

[§]To whom correspondence should be addressed. E-mail: kendall.knight@umassmed.edu.

© 2006 by The National Academy of Sciences of the USA

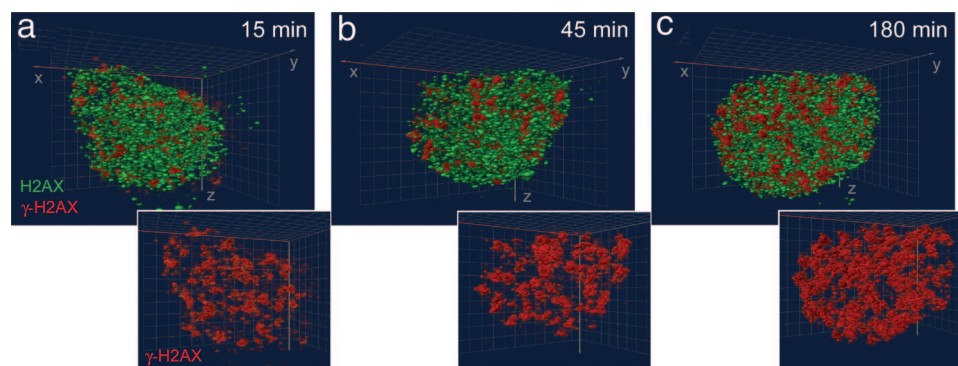


Fig. 1. 4Pi images of H2AX and γ -H2AX clusters during a time course of DNA damage and repair. HeLa cells exposed to 3 Gy IR were fixed 15, 45, and 180 min after irradiation and immunolabeled with γ -H2AX (red) and H2AX (green) antibodies. Images were obtained by using a 4Pi microscope and deconvolved. 3D-rendered 4Pi data for the 15, 45, and 180 min after IR time points are displayed in *a*, *b*, and *c*, respectively. (Insets) γ -H2AX data alone. Movies for all time points after IR (15, 45, 90, 180, 360, and 720 min) are presented in Movies 1–6.

3D Nuclear Distribution of H2AX and γ -H2AX Clusters. The 3D distribution throughout the nucleus of both H2AX and γ -H2AX clusters was quantified by measuring their fluorescence intensity recorded by a confocal microscope within a series of 3D shells of 400-nm thickness characterized by their distance to the nuclear periphery (Fig. 3; see Fig. 7, which is published as supporting information on the PNAS web site). Examples of the raw confocal data used for the calculations are displayed in Fig. 3 (Fig. 3 *a–d*; DAPI, H2AX, γ -H2AX and overlay, respectively). The nuclear dimensions were determined by using smoothed DAPI data (Fig. 3*e*) and nonoverlapping 3D shells of 400-nm thickness, differing by their distance to the nuclear border (multiples of 400 nm), were derived (Fig. 3*f*). For all individual points in the time course, we find that the H2AX and γ -H2AX levels remain on average constant throughout the entire nuclear volume (Figs. 3 *g–i* and 7). This supports a model in which DSBs can occur in any region of the nucleus and are likely to be processed and repaired in the area where they arise. It has been proposed that in yeast, multiple DSBs may accumulate at repair

centers (18). However, in accord with recently published work (17), the fact that we find γ -H2AX clusters appearing throughout the entire nuclear volume argues against the ideas that specific repair centers exist in mammalian nuclei or that DNA repair takes place preferentially near the nuclear periphery or center. This suggests that γ -H2AX simply serves as a mark for both the recruitment and retention of signaling and repair factors required to mount an appropriate response to DNA damage (2, 19), irrespective of its nuclear location. Consistent with a general increase in the amount of γ -H2AX immediately after exposure to IR, we find that the γ -H2AX/H2AX ratio increases on average 5-fold within the first 15 min after exposure to IR (Fig. 3 *g* and *h*). We also observe an overall decrease in the level of γ -H2AX fluorescence at 360 and 720 min after IR (Fig. 3*i* and Fig. 7 *f* and *g*). Related approaches have been used to provide information regarding the radial distribution of proteins within the nucleus (20, 21), but the new algorithm used for our analysis provides insight into the steady-state localization in 3D and stress-induced changes in the distribution of γ -H2AX throughout the nuclear volume.

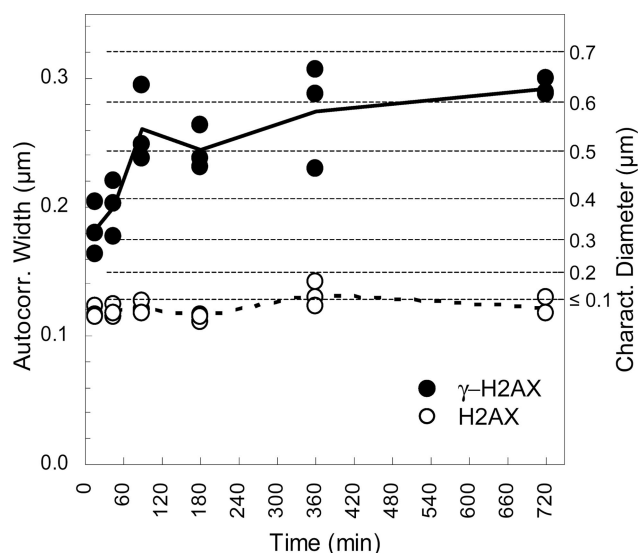


Fig. 2. Cluster size as a function of time after DNA damage. The characteristic size of both H2AX and γ -H2AX clusters were determined for each time point during DNA repair by using the autocorrelation function of the deconvolved 4Pi data (see *Supporting Materials and Methods*). Whereas the H2AX clusters remain at subresolution size during the whole time course, the characteristic size of γ -H2AX clusters increases 2-fold reaching a plateau after \approx 90 min.

Lack of Coincident Staining of H2AX and γ -H2AX. We observe no significant coincident staining for H2AX and γ -H2AX at any time after exposure to IR. This was quantified by analyzing the cross-correlation of the voxel values of both channels in the 3D 4Pi data sets. Representative cuts through a deconvolved 4Pi 3D data set are shown in Fig. 4*a*. The results of the cross-correlation analysis are displayed by using a 2D cytofluorogram (Fig. 4*b*) in which the horizontal axis corresponds to the signal level of the H2AX channel (green) and the vertical axis to the γ -H2AX channel signal (red). Using a logarithmic color table, the entire dynamic range of the cytofluorogram could be visualized. The cytofluorogram consists mainly of two lobes oriented in horizontal and vertical directions and shows very little signal in the region between the lobes, thus ruling out significant colocalization. To investigate possible colocalization in more detail, the cytofluorogram counts in the area between the two lobes were analyzed further by comparing profiles parallel to the vertical lobe at different horizontal positions (dotted lines in Fig. 4*b* and profiles in Fig. 4*b* *Inset*). All profiles show the same shape and differ only in the number of counts (profiles have been normalized to their maximum values shown in the Fig. 4*b* *Inset*: 3,900; 200; 24). The same behavior can be observed for profiles along the horizontal direction. Because even minor amounts of systematic colocalization would result in a peak or shoulder with varying positions in the different profiles, this indicates that no significant colocalization occurs. The small number of counts observed in the area between the lobes is consistent with the

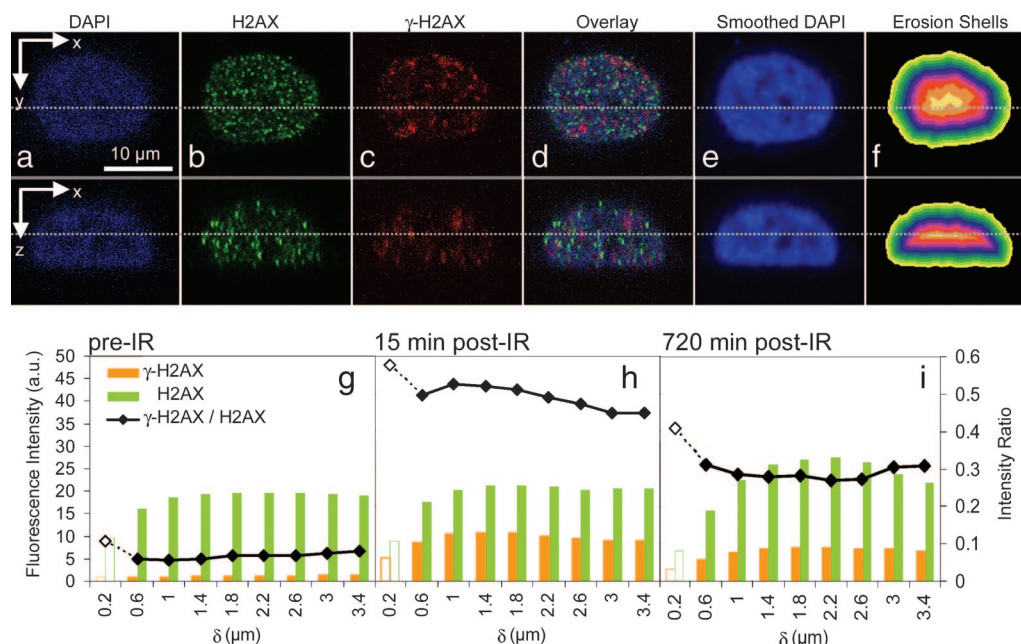


Fig. 3. 3D distribution of H2AX and γ -H2AX clusters in the nuclear volume. Fluorescence intensities of both the γ -H2AX (red) and H2AX (green) channels were analyzed in 3D (confocal data are used for this analysis because the microscope collects three channels, whereas the 4Pi instrument collects only two). Examples of xy and xz sections of 3D data sets showing the DAPI (a), H2AX (b), γ -H2AX (c), and overlay (d) signals used for the calculations are shown. Nuclear dimensions were determined by creating a series of shells shown in different colors (f) based on eroding smoothed DAPI stain images (e) in 400-nm steps (see *Supporting Materials and Methods*). Histograms for $t = 0$ (g), 15 (h), and 720 (i) min after IR averaged over 10–11 cells are displayed (SE ranges from 5% to 20%) and show a time-dependent change in fluorescence intensity for the γ -H2AX signal (red) and little change in the intensity of the H2AX signal. Both intensities show little to no dependence on the distance from the nuclear periphery (j). (g–j) Because of an inaccuracy in the identification of the nuclear boundary, defined by a smoothed DAPI signal threshold, a continuous rise in the signal for the first two shells instead of a step-like rise is observed. For the ratios shown between γ -H2AX and H2AX, this cancels out.

purely coincidental occurrence of separate H2AX and γ -H2AX clusters in a distance closer than or at the resolution limit of the microscope (see *Supporting Materials and Methods*). The fact that we observe no mixed populations of H2AX and γ -H2AX signals means that phosphorylation of virtually all of the H2AX within a given cluster spreads very rapidly after DNA damage and is essentially complete before 15 min. This agrees with previous biochemical studies showing that H2AX phosphorylation is complete within 10–20 min after DNA damage (3). To eliminate

the possibility that staining with the first antibody combination may sterically hinder access of the second, we found that the appearance of H2AX and γ -H2AX clusters was identical regardless of which was stained first (data not shown). Additional controls in which the secondary antibody fluorescent conjugates were switched such that H2AX appears red and γ -H2AX green (Fig. 8, which is published as supporting information on the PNAS web site), demonstrate the specificity of cluster appearance and rule out any instrumental or preparative artifacts.

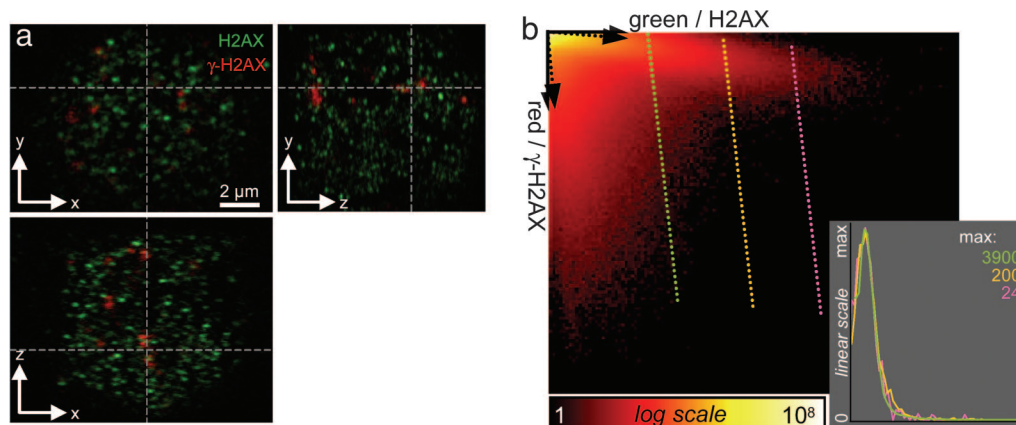


Fig. 4. Lack of colocalization of H2AX and γ -H2AX staining throughout the nuclear volume. (a) Sections in all directions through a typical 3D 4Pi data set show no significant overlap between the red (γ -H2AX) and green (H2AX) signals (dashed lines represent positions of different sections). Analysis of all data sets by cytofluorograms (example shown in *b*) reveals a minimal signal overlap (note the logarithmic color scale). (b and *b Inset*) Profiles in *b Inset* represent the cytofluorogram data along the dotted lines in *b*. The fact that they are the same shape agrees with the expected coincidental overlap of the resolution-limited signals. The profiles were normalized according to the numbers displayed in *b Inset*. The dotted arrows (upper left in *b*) indicate the directions for the cross-talk corrected signal (see *Supporting Materials and Methods*).

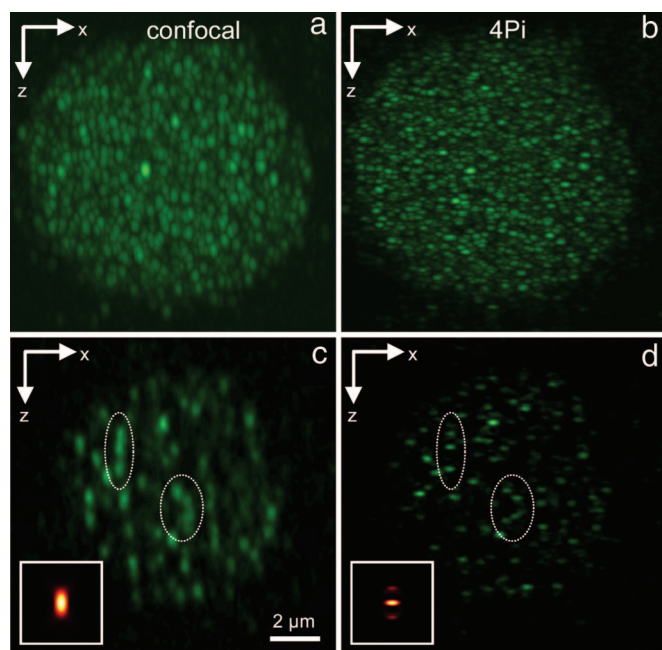


Fig. 5. Comparison of confocal vs. 4Pi microscopy for endogenous human histone H2AX. (a and b) The data shown represent the H2AX staining in a HeLa cell nucleus as seen with confocal and 4Pi microscopy, respectively, in a maximum projection of 3D data sets. (c and d) The same single xz section taken from the 3D data sets of a and b, respectively. The dotted ellipses mark areas where the resolution enhancement can be seen best. (c Inset and d Inset) The PSFs of confocal and 4Pi microscopy at the same scale as a–d for comparison.

The absence of coincident staining of H2AX and γ -H2AX at later times in the repair process, e.g., 360 and 720 min, is consistent with the idea that dephosphorylation of γ -H2AX occurs only after its removal from nucleosomes, and that it is not simply swapped for another molecule of unphosphorylated H2AX. In fact, recent studies show that *Saccharomyces cerevisiae* Pph3 phosphatase targets γ -H2AX after its displacement from DNA (22). This idea also is supported by our observation that the characteristic γ -H2AX cluster size remains fairly constant from 6 to 12 h after IR (Fig. 2), yet the overall fluorescence intensity appears to decrease at these later times (Fig. 7f and g). The latter observation also suggests that loss of the γ -H2AX signal, whether by phosphatase action or by direct removal of γ -H2AX from nucleosomes (22–24), occurs randomly within a given cluster. This is different from the model for directional spreading of the DNA damage-induced phosphorylation of H2AX, which is best shown by chromatin immunoprecipitation (25) and supported by immunofluorescence data (17, 26).

Discussion

Recent studies suggest that DSB processing causes a local expansion of chromatin in the region of the break. Although γ -H2AX is not required for the initial ATP-dependent expansion, it was speculated that it is essential to sustain chromatin decondensation as DNA repair progresses, thereby providing a link between the expanded chromatin region and the localized spread of γ -H2AX (17). Our data now suggest that the size of H2AX clusters and distance between them serves to limit spreading of γ -H2AX and associated chromatin expansion. The average number of H2AX clusters observed in our images both before DNA damage and at all times after damage approximates 5,000 (see *Supporting Materials and Methods*). In a diploid nucleus, the 6×10^9 bp of DNA would be accommodated by ≈ 30 million nucleosomes (200 bp DNA per nucleosome). Assuming

a cylindrical shape of 6 nm height and 5.5 nm radius for a nucleosome (570 nm^3), 30 million would occupy $\approx 17 \mu\text{m}^3$, or 3.3% of the total nuclear volume of a 10- μm diameter HeLa nucleus. In the possible scenario that H2AX is distributed randomly throughout the genome and that all nucleosomes are accounted for by the 5,000 clusters we observe, $\approx 6,000$ nucleosomes should be related to each cluster. This number of nucleosomes corresponds to ≈ 1.2 Mbp of DNA, and we note that this closely matches estimates of the amount of DNA in which H2AX phosphorylation spreads from a break in mammalian cells (3, 16). However, our analysis shows that H2AX clusters have a diameter near the resolution limit of 4Pi microscopy ($\approx 100 \text{ nm}$) and, thus, could accommodate a maximum of only 900 closely packed nucleosomes each. Therefore, only up to 15% of total nucleosomes can be located in the clusters. This suggests that nucleosomes containing H2AX are not distributed uniformly throughout bulk chromatin, rather they are concentrated within the 100-nm diameter clusters. Thus, although H2AX represents 2.4% of the total H2A in HeLa cells (3), the fractional amount of H2AX within a cluster would be significantly higher. These observations could be accommodated by higher-order chromatin structures proposed to contain on the order of 1–2 Mbp DNA in which chromatin loops emanate from a central region (27, 28) where H2AX would be concentrated. We propose that the H2AX clusters observed here by using 4Pi microscopy may correspond to the central region of these higher-order structures. In further studies, we will analyze the localization of H2AX relative to other chromatin components. Therefore, our current data support a model in which spreading of H2AX phosphorylation in response to DNA damage is constrained by structures defined by these H2AX clusters. The subsequent increase in size of the γ -H2AX clusters between 20 and 100 min after DNA damage may result from localized chromatin expansion (4–6, 17) and increased flexibility due to resection of one DNA strand without concomitant loss of nucleosomes (25). Although a localized aggregation of proximal DSBs may contribute in part to this (26), our data suggest that this does not involve large-scale chromatin movement. Additionally, the local concentration of H2AX within these clusters, which themselves are uniformly distributed throughout the nuclear volume, may contribute to the immediate and robust response of signaling and repair proteins after DNA damage.

This study represents a significant advance in our ability to visualize and quantify endogenous nuclear proteins in 3D. Combined, these methods have allowed us to visualize a chromatin structure at the 100-nm resolution level and to quantify the size and distribution of both H2AX and γ -H2AX clusters in response to DNA damage. The general application of these methods will provide unprecedented insights into cellular molecular events and now specifically events related to the maintenance of genome integrity and most aspects of nuclear metabolism.

Materials and Methods

Antibodies. Primary antibodies were mouse monoclonal anti- γ -H2AX (phospho-Ser-139) (clone JBW301, catalog no. 06-636; Upstate Biotechnology, Charlottesville, VA) and rabbit polyclonal anti-H2AX (Upstate Biotechnology; catalog no. 07-627). Rabbit polyclonal anti-H2AX was protein-A purified by us, whereas monoclonal anti- γ -H2AX was purified by Upstate Biotechnologies, and purification was verified by Coomassie-stained protein gel. Immunofluorescence detection was achieved by using Alexa Fluor 488 goat anti-mouse IgG (H+L, no. A-11029; Invitrogen, Carlsbad, CA), Alexa Fluor 488 goat anti-rabbit IgG (H+L, no. A-11034; Invitrogen), Alexa Fluor 647 goat anti-mouse IgG (H+L, no. A-21236; Invitrogen), Rhodamine Red-X goat anti-rabbit IgG (H+L, no. R-6394; Invitrogen), or Rhodamine Red-X goat anti-mouse IgG (H+L,

no. R-6393; Invitrogen), all of which are highly cross-absorbed. All primary and secondary antibodies were applied at a 1:500 dilution in blocking buffer containing 20% marine blocking agent in PBS. For conventional confocal microscopy, cells were mounted in Vectashield Fluorescent Mounting Media containing DAPI (Vector Laboratories, Burlingame, CA). For 4Pi microscopy, cells were mounted in a solution of 87% glycerol in 130 mM Tris-HCl (pH 7.4).

Cells and Damage-Induced DNA DSBs. HeLa cells from American Type Culture Collection were maintained in DMEM with 10% FBS/1% penicillin/streptomycin. Cells were grown to ~80% confluency, in an atmosphere containing 5% CO₂ at 37°C. Cells were exposed to 3 Gy IR (¹³⁷Cs) by using a Gammacell 40 (MDS Nordion) and were incubated at 37°C (5% CO₂) for the indicated times.

4Pi vs. Confocal Imaging of Histones H2AX and γ -H2AX. Type C 4Pi microscopy covers twice the solid angle of standard (confocal) microscopy (2.7 π with the objectives used) for both excitation and detection by combining the wavefronts of two high numerical aperture (NA) objective lenses coherently (13, 14, 29). For constructive interference, the favorable opposing lens arrangement realized results in a focal volume or point-spread function (PSF) with a central peak of ~100-nm width FWHM, 5- to 7-fold improved in comparison with regular confocal PSFs (Fig. 5). Imaging nuclear structures with interference microscopy techniques such as 4Pi microscopy is potentially difficult: Wavefront distortions in the vicinity of cell nuclei that degrade the 4Pi PSF have been reported (15). However, by matching the cytosolic and nuclear refractive indices by glycerol-embedding the sample and using 1.35 NA glycerol immersion lenses (30) with the embedding medium for immersion, we found that refractive indices could be matched for HeLa cells. In fact, the high quality of the PSFs enabled removal of the ghost images produced by the axially shifted side-maxima in the 4Pi PSF by simple linear 5-point deconvolution (31). The improved resolution achieved by 4Pi microscopy compared with standard confocal microscopy of the same sample is shown in Fig. 5 with the insets comparing the PSFs of confocal (Fig. 5c) vs. 4Pi (Fig. 5d) microscopes.

Confocal Microscopy. Cells were grown on poly-D-lysine-treated glass coverslips in a six-well dish to ~80% confluency before exposure to IR. After exposure, cells were removed from the incubator at appropriate times for fixation. Growth medium was aspirated from the wells, cells were quickly rinsed in room temperature PBS, and then immediately were immersed in 100% methanol at -20°C for 7 min. Cells were blocked in a marine blocking agent overnight at 4°C and washed once in PBS (5 min at room temperature). Incubation with primary and secondary antibodies was performed in six-well dishes in a humid environment (Fisher slide warmer, 37°C for 90 min each). Cells were washed three times in PBS (10 min each) after incubation with each primary antibody and five times in PBS (10 min each) after incubation with each secondary antibody. For all double-staining procedures, cells were stained in a sequential manner as opposed to using antibody cocktails. For example, cells were incubated

first with anti- γ -H2AX followed by incubation with the secondary Alexa Fluor 647. Subsequently, cells were incubated with anti-H2AX followed by its appropriate secondary, Alexa Fluor 488. The choice of Alexa Fluor 488 and Alexa Fluor 647 was purposeful, in that there is little to no cross-talk in the emission and excitation of this fluorophore pair, all but eliminating the possibility of artificial colocalization patterns. Coverslips were mounted by using Vectashield with DAPI and sealed with polyurethane (nail polish). Samples then were stored in the dark at 4°C. 3D data sets were recorded by using a TCS SP2 AOBs confocal microscope (Leica Microsystems). Further details regarding confocal imaging and data collection are provided in *Supporting Materials and Methods*.

4Pi Microscopy. 4Pi samples were prepared between two opposing quartz coverglasses that are matched in width at 220 μ m (\pm 5 μ m). The upper coverslip, on which the cells were grown, was acid etched (70% ethanol/1% hydrochloric acid in PBS) for 5 min, washed three times in PBS (room temperature), and bathed in DMEM with poly-D-lysine (1 mg/ml) for 1 h at room temperature. Slips then were washed once in DMEM followed by two washes in DMEM containing 10% FBS and 1% penicillin/streptomycin and seeded with cells. The lower coverslip that contains a transparent center surrounded by a mirror reflective surface was not treated by acid etching or poly-D-lysine. The lower coverslip mirror can be used in adjusting the two wavefronts in the reflective mode of the 4Pi system. Cells were fixed and stained as described above for confocal imaging, except that a Rhodamine Red-X secondary antibody was used to stain the γ -H2AX. Mounting of 4Pi coverslips is achieved by placing the lower slip (mirrored surface) into the 4Pi sample holder, a round metal ring with an indentation to match the quartz coverslip. The lower slip is adhered to the sample holder by using polyurethane (nail polish). Once dried, 40 μ l of an 87% glycerol in 130 mM Tris-HCl (pH 7.4) embedding media was added to the lower slip. The upper slip was removed from the PBS of the last wash, allowed to air dry briefly and added to the lower coverslip, sandwiching the cells between the two opposing quartz slips. Samples were sealed with nail polish and stored in the dark at 4°C. Further details regarding 4Pi imaging and data collection are provided in *Supporting Materials and Methods*.

Quantification of Cluster Parameters. Detailed descriptions of methods and outlines of algorithms used to calculate (i) potential colocalization of H2AX and γ -H2AX fluorescent signals, (ii) cluster number, (iii) cluster size, and (iv) cluster spatial distribution during the time course after DNA damage are provided in the *Supporting Materials and Methods*.

We thank M. Lessard and S. Douthwright for technical assistance; J. Bone and C. Kier for support; and B. Knowles, M. Handel, C. Peterson, and O. Gildemeister for comments on the manuscript. This work was supported by Department of Defense Breast Cancer Research Program Predoctoral Fellowship W81XWH-04-1-0601 (to B.T.B.) and National Institutes of Health Grants GM44772 and GM65851 (to K.L.K.). Funding for the 4Pi confocal laser scanning microscope was provided by the W. M. Keck Foundation and National Science Foundation Grant DBI-0421007 (to The Jackson Laboratory).

- O'Driscoll M, Jeggo PA (2006) *Nat Rev Genet* 7:45–54.
- Stucki M, Jackson SP (2006) *DNA Repair* 5:534–543.
- Rogakou EP, Pilch DR, Orr AH, Ivanova VS, Bonner WM (1998) *J Biol Chem* 273:5858–5868.
- Thiriet C, Hayes JJ (2005) *Mol Cell* 18:617–622.
- Peterson CL, Cote J (2004) *Genes Dev* 18:602–616.
- Nussenzweig A, Paull T (2006) *Nature* 439:406–407.
- Kim JS, Krasieva TB, LaMorte V, Taylor AM, Yokomori K (2002) *J Biol Chem* 277:45149–45153.
- Strom L, Lindroos HB, Shirahige K, Sjogren C (2004) *Mol Cell* 16:1003–1015.

- Unal E, Arbel-Eden A, Sattler U, Shroff R, Lichten M, Haber JE, Koshland D (2004) *Mol Cell* 16:991–1002.
- Nelms BE, Maser RS, MacKay JF, Lagally MG, Petrini JH (1998) *Science* 280:590–592.
- Bennett BT, Knight KL (2005) *J Cell Biochem* 96:1095–1109.
- Bekker-Jensen S, Lukas C, Melander F, Bartek J, Lukas J (2005) *J Cell Biol* 170:201–211.
- Hell S, Stelzer EH (1992) *Opt Commun* 93:277–282.
- Gugel H, Bewersdorf J, Jakobs S, Engelhardt J, Storz R, Hell SW (2004) *Biophys J* 87:4146–4152.

15. Egner A, Verrier S, Goroshkov A, Soling HD, Hell SW (2004) *J Struct Biol* 147:70–76.
16. Rogakou EP, Boon C, Redon C, Bonner WM (1999) *J Cell Biol* 146:905–916.
17. Kruhlak MJ, Celeste A, Dellaire G, Fernandez-Capetillo O, Muller WG, McNally JG, Bazett-Jones DP, Nussenzweig A (2006) *J Cell Biol* 172:823–834.
18. Lisby M, Mortensen UH, Rothstein R (2003) *Nat Cell Biol* 5:572–577.
19. Fernandez-Capetillo O, Celeste A, Nussenzweig A (2003) *Cell Cycle* 2:426–427.
20. Irinopoulou T, Vassy J, Beil M, Nicolopoulou P, Encaoua D, Rigaut JP (1997) *Cytometry* 27:99–105.
21. Knowles DW, Sudar D, Bator-Kelly C, Bissell MJ, Lelievre SA (2006) *Proc Natl Acad Sci USA* 103:4445–4450.
22. Keogh MC, Kim JA, Downey M, Fillingham J, Chowdhury D, Harrison JC, Onishi M, Datta N, Galicia S, Emili A, *et al.* (2006) *Nature* 439:497–501.
23. Chowdhury D, Keogh MC, Ishii H, Peterson CL, Buratowski S, Lieberman J (2005) *Mol Cell* 20:801–809.
24. Bouquet F, Muller C, Salles B (2006) *Cell Cycle* 5:1116–1122.
25. Shroff R, Arbel-Eden A, Pilch D, Ira G, Bonner WM, Petrini JH, Haber JE, Lichten M (2004) *Curr Biol* 14:1703–1711.
26. Aten JA, Stap J, Krawczyk PM, van Oven CH, Hoebe RA, Essers J, Kanaar R (2004) *Science* 303:92–95.
27. Munkel C, Eils R, Dietzel S, Zink D, Mehring C, Wedemann G, Cremer T, Langowski J (1999) *J Mol Biol* 285:1053–1065.
28. Huebert DJ, Bernstein BE (2005) *Curr Opin Genet Dev* 15:476–481.
29. Hell SW (1990) Eur Patent 0491289.
30. Martini N, Bewersdorf J, Hell SW (2002) *J Microsc* 206:146–151.
31. Medda R, Jakobs S, Hell SW, Bewersdorf J (September 7, 2006) *J Struct Biol*, 10.1016/j.jsb. 2006.08.013.